Optics Letters

Frequency manipulation of topological surface states by Weyl phase transitions

Zhuoxiong Liu,[1] Chengzhi Qin,[1,3] Weiwei Liu,[1] Lingzhi Zheng,[1] Shuaifei Ren,[1] Bing Wang,[1,*] and Peixiang Lu[1,2,4]

[1]*School of Physics and Wuhan National Laboratory for Optoelectronics, Huazhong University of Science and Technology, Wuhan 430074, China*
[2]*Hubei Key laboratory of Optical Information and Pattern Recognition, Wuhan Institute of Technology, Wuhan 430025, China*
[3]*e-mail: qinchengzhi@hust.edu.cn*
[4]*e-mail: lupeixiang@hust.edu.cn*
Corresponding author: wangbing@hust.edu.cn

By creating a synthetic frequency dimension with dynamic modulation in a 2D honeycomb waveguide array, we construct both Type-I and Type-II Weyl semimetals (WSMs) and utilize the WSM phase transition to control the frequency evolutions of topological surface states. We show that Type-I WSMs and Type-II WSMs manifest opposite and same band slopes for the two surface states, which give rise to the bidirectional and unidirectional frequency shifts, respectively. Moreover, by cascading Type-I Weyl lattices and Type-II Weyl lattices together, we also achieve the time-reversed evolution of frequency, such as frequency negative refraction, bandwidth expansion-compression, and perfect imaging. The Letter may find applications in robust signal transmission and processing with synthesized topological states. © 2021 Optical Society of America

https://doi.org/10.1364/OL.442890

Weyl semimetals (WSMs), possessing three-dimensional (3D) band degeneracy points, have emerged as new topological states both in condensed-matter and classical-wave systems [1–6]. Basically, WSMs can be classified into two types: Type-I, which has a standard point-like Fermi surface, and Type-II, which has a tilted spectrum appearing at the contact of electron and hole pockets [7], giving rise to different transport dynamics and chiral anomaly effects [8,9]. Current researches on photonic WSMs mainly focus on static 3D spatial lattices, where photon frequency is a conserved quantity. Generally, the ability to control the frequency of light is desirable both for fundamental research and practical applications [10–13]. Present studies on frequency control are mainly limited to trivial photonic states in waveguides, resonators, etc. [14–16]. However, the manipulation of frequency for topological edge and surface states is also useful in the robust light transmission and signal processing, which still remains elusive.

Recently, the conception of synthetic frequency dimension, as proposed in dynamic modulated systems, provides a new method to control the frequency of light [14,17]. The frequency dimension can not only be utilized to emulate higher-dimensional topological physics using lower-dimensional

structures, but also provides a platform to control the frequency evolution of topological states [18]. Particularly, by adding a frequency dimension in a 2D spatial lattice, photonic WSMs have been created and one-way frequency conversion of topological surface states have been achieved [19,20]. However, previous works have not revealed the mechanism of how the WSM types control the surface state frequency evolutions. From practical perspective, the time-reversal evolution of frequency, such as frequency negative refraction, is desirable in the applications of spectrum reconstruction and signal processing, which also can't be realized in previously studied single-type WSMs.

In this Letter, we construct both Type-I WSMs and Type-II WSMs in a single Weyl lattice and achieve versatile frequency evolutions of topological surface states. The Weyl lattice is created based on a dynamically modulated 2D honeycomb waveguide array, where the modulation can create an additional frequency dimension. By choosing appropriate modulation amplitudes and phases, both Type-I WSM phases and Type-II WSM phases can be achieved. Accordingly, the frequency evolution of the surface states pair in a truncated lattice is determined by the type, which exhibit opposite frequency shifts for Type-I and same shifts for Type-II. What's more, by cascading two Weyl lattices of different types, we also achieve time-reversed evolutions of surface states, such as frequency negative refraction, bandwidth expansion and compression and perfect imaging.

Consider the Type-I WSMs and Type-II WSMs created in a dynamically modulated waveguide array. As shown in Fig. 1(a), each sub-lattice A and sub-lattice B in a honeycomb array is subjected to a traveling-wave refractive index modulation $n_{A(B)} = n_0 + \Delta n_{A(B)} \cos[\Omega t - qz + \phi_{A(B)}]$, where n_0, $\Delta n_{A(B)}$, Ω, q, and $\phi_{A(B)}$ are the background refractive index, the modulation amplitude, the frequency, the wavenumber and initial phases in A and B, respectively. The modulation can induce photonic transitions among a set of modes with a frequency interval Ω, thus forming a synthetic frequency lattice [14]. The frequency lattice and the 2D waveguide array constitute a synthetic 3D lattice, as shown in Fig. 1(b), which can be described by the tight-binding Hamiltonian
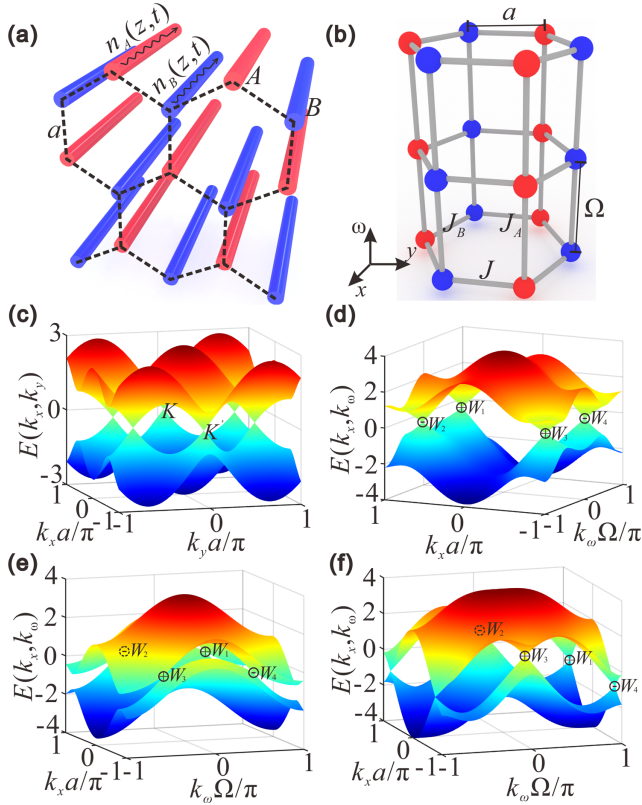
Fig. 1. (a) Schematic of a dynamically modulated honeycomb waveguide array. $n_{A(B)}(z, t)$ denotes the refraction index modulation in A (red) and B (blue) waveguides. (b) Synthetic 3D lattice consisting of the in-plane honeycomb lattice and a perpendicular frequency lattice with lattice constants of a and Ω and coupling strengths of J and $J_{A(B)}$, respectively. (c) Honeycomb lattice band structure with two Dirac points, $K = (4\pi/3\sqrt{3}a, 0)$ and $K' = (-4\pi/3\sqrt{3}a, 0)$. (d) (e) Type-I and Type-II band structures for P-broken case. (f) Type-I band structure for T-broken case. $W_i (i = 1, 2, 3, 4)$ represent the WPs with "+ (−)" denoting its chirality.

$$H = \sum_{i,n} J(a^+_{r_i,n} b_{r_i+\rho_1,n} + a^+_{r_i,n} b_{r_i+\rho_2,n} + a^+_{r_i,n} b_{r_i+\rho_3,n} + \text{h.c.})$$

$$+ \sum_{i,n} J_A(a^+_{r_i,n} a_{r_i,n+1} e^{-i\phi_A} + \text{h.c.})$$

$$+ \sum_{j,n} J_B(b^+_{r_j,n} b_{r_j,n+1} e^{-i\phi_B} + \text{h.c.}),$$

$$\text{(1)}$$

where $a^+_{r_i,n} (a_{r_i,n})$, $b^+_{r_i,n}(b_{r_i,n})$ are creation (annihilation) operators for the modes in waveguide A and waveguide B with frequency $\omega_n = \omega_0 + n\Omega$, $n = 0, \pm1, \pm2 \dots$ is the site index in the frequency lattice. $\rho_1 = (\sqrt{3}a/2, a/2)$, $\rho_2 = (-\sqrt{3}a/2, a/2)$, and $\rho_3 = (0, -a)$, with a being the in-plane lattice constant. J is the in-plane coupling coefficient. J_A, J_B and ϕ_A, ϕ_B are the frequency-domain coupling strengths and phases.

Through Fourier transformation, we can obtain the Bloch Hamiltonian

$$H(k) = [J_A \cos(k_\omega\Omega - \phi_A) + J_B \cos(k_\omega\Omega - \phi_B)]\sigma_0$$

$$+ [J_A \cos(k_\omega\Omega - \phi_A) - J_B \cos(k_\omega\Omega - \phi_B)]\sigma_z$$

$$+ H_{2D}(k_x, k_y), \quad \text{(2)}$$

where k_x, k_y, and k_ω are Bloch momenta along x, y, and frequency axes. σ_0 is the 2×2 identity matrix and $\sigma_i (i = x, y, z)$ are the Pauli matrices. The $H_{2D}(k_x, k_y)$ is got from the first term of Eq. (1), which can support two Dirac points $K = (4\pi/3\sqrt{3}a, 0)$ and $K' = (-4\pi/3\sqrt{3}a, 0)$ in the 2D Brillouin zone, as shown in Fig. 1(c), which can be extended to Weyl points (WPs) under the appropriate modulations by breaking either parity (P) or time-reversal (T) symmetry [3,7]. Throughout the paper, we only consider two special cases of breaking only P or T. Breaking both P and T can also give rise to two types of WSMs and same surface state evolutions, which will not be discussed here. Specifically, to break P and preserve T, we set $J_A \neq J_B$ and $\phi_A = 0$, $\phi_B = \pi$ or $\phi_A = 0$, $\phi_B = 0$. To break T and preserve P, we set $J_A = J_B$, $\phi_A = -\phi_B \neq 0$ and π.

First, we consider the P-broken case. The four WPs are located at $(k_{x0}, k_{y0}, k_{\omega0}) = (\pm4\pi/3\sqrt{3}a, 0, \pm\pi/2\Omega)$, near one of which $(4\pi/3\sqrt{3}a, 0, \pi/2\Omega)$, the effective Hamiltonian and energy spectrum are

$$H(q) = v_x q_x \sigma_x + v_y q_y \sigma_y$$

$$+ \begin{cases} (v_0 q_\omega \sigma_0 + v_\omega q_\omega \sigma_z), & (\phi_A = 0, \phi_B = \pi) \\ (v_\omega q_\omega \sigma_0 + v_0 q_\omega \sigma_z), & (\phi_A = 0, \phi_B = 0) \end{cases}, \quad \text{(3)}$$

$$E(q) =$$

$$\begin{cases} v_0 q_\omega \pm \sqrt{(v_x q_x)^2 + (v_y q_y)^2 + (v_\omega q_\omega)^2}, & (\phi_A = 0, \phi_B = \pi) \\ v_\omega q_\omega \pm \sqrt{(v_x q_x)^2 + (v_y q_y)^2 + (v_0 q_\omega)^2}, & (\phi_A = 0, \phi_B = 0) \end{cases},$$

$$\text{(4)}$$

where "$\pm$" denotes the two bands, $q_i = k_i - k_{0i}$ ($i = x, y, \omega$), $v_x = -3Ja/2$, $v_y = 3Ja/2$, $v_0 = -(J_A - J_B)\Omega$, and $v_\omega = -(J_A + J_B)\Omega$. Specifically, for $q_x = q_y = 0$, the energy spectrum is

$$E(q) = \begin{cases} (v_0 \pm v_\omega)q_\omega, & (\phi_A = 0, \phi_B = \pi) \\ (v_\omega \pm v_0)q_\omega. & (\phi_A = 0, \phi_B = 0) \end{cases}, \quad \text{(5)}$$

which gives rise to the frequency-dimension group velocities $v_g = \partial E(q)/\partial q_\omega$. Since $|v_0| < |v_\omega|$, the group velocities of the two bands are opposite for $\phi_A = 0$, $\phi_B = \pi$ while the same for $\phi_A = 0$, $\phi_B = 0$, satisfying the conditions of Type-I WPs and Type-II WPs [7]. Figures 1(d) and 1(e) show the band structures $E(k_x, k_\omega)$ at $k_y = 0$, obtained from the Eq. (2), which clearly show the point-like and tilted energy spectra, respectively. For the T-broken case, with similar procedure, we can also get the effective Hamiltonian and energy spectrum

$$\begin{cases} H(q) = E_0\sigma_0 + v'_\omega q_\omega \sigma_z + v_x q_x \sigma_x + v_y q_y \sigma_y, \\ E(q) = E_0 \pm \sqrt{(v_x q_x)^2 + (v_y q_y)^2 + (v'_\omega q_\omega)^2}, \end{cases} \quad \text{(6)}$$

where $E_0 = 2J_\omega \cos\phi$ and $v'_\omega = 2J_\omega\Omega\sin\phi$. Figure 1(f) shows band structure calculated using Eq. (2) for T-broken case. The bands have opposite slopes near WPs, which is the signature of the Type-I WPs.
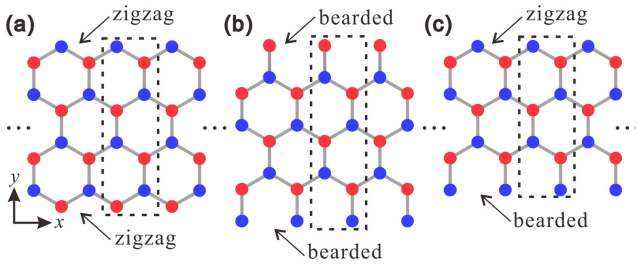
Fig. 2. Schematic diagrams of three truncated lattices: (a) "zz", (b) "bb", and (c) "zb" lattices. Each black dashed rectangle represents the unit cell for the truncated honeycomb lattice.

Next, we truncate the lattice along y axis and keep periodicities along x and ω axes, such that Fermi-arc surface states will emerge on the "x-ω" plane [21]. For honeycomb lattice to exhibit edge states, there require two types of edges, i.e., zigzag and bearded edges, through the combination of which there are totally three types of truncated lattices: "zigzag-zigzag (zz)," "bearded-bearded (bb)," and "zigzag-bearded (zb)," as shown in Fig. 2. Since the Fermi arcs of the "zz" and "bb" lattices are distributed at complementary positions in the Brillouin zone [22], they share the same surface states evolution behaviors. Below, we choose "zz" and "zb" lattices for detailed discussions.

Figures 3(a) and 3(b) show the sliced projected band structures $E(k_\omega)$ of "zz" lattice [see Fig. 2(a)] for the P-broken case with $k_x = 0.85\pi/\sqrt{3}a$ for $J_A = 1$, $J_B = 0.5$, $\phi_A = 0$, $\phi_B = \pi$ and $\phi_A = 0$, $\phi_B = 0$, respectively. The black curves are bulk bands, and the red, blue curves denote the two surface states at the top and bottom edges. Remarkably, in the entire Brillouin zone, the band slopes of the two surface states are always opposite in Fig. 3(a) and the same in Fig. 3(b), which are the clear signatures for the Type-I WSMs and Type-II WSMs. Accordingly, the two surface states will propagate along the opposite (same) directions in the frequency dimension. Also note that the amplitudes of the two band slopes are different for both Type-I WSMs and Type-II WSMs. For the T-broken case with $J_A = J_B = 1$ and $\phi_A = -\phi_B = \pi/3$, the sliced projected band structure $E(k_\omega)$ is shown in Fig. 3(c). The band slopes for T-broken case depend on the choice of Bloch momentum, which are opposite for $0 < k_\omega < \pi/3\Omega$ and the same for $\pi/3\Omega < k_\omega < 2\pi/3\Omega$. Specifically, at the critical points $k_\omega = \pi/3\Omega$ or $2\pi/3\Omega$, the group velocity of one surface state vanishes. Figure 3(d) displays the sliced projected band structure of the "zb" lattice [see Fig. 2(c)], which exhibits only one surface state. The frequency evolution is only determined by the central Bloch momentum of inject packet.

To visualize how the WSM types control the frequency evolutions of two surface states, we inject a frequency-domain wave packet into the two edges. Figures 4(a) and 4(b) show the wave packet evolutions of the two surface states for P-broken case. Here the frequency shift $\Delta\omega$ is normalized by the modulation frequency Ω. The wave packet carries a central Bloch momentum $k_\omega = 0.508\pi/\Omega$ and Gaussian envelope of width $W = 5\Omega$ truncated at 5-th order. As shown in Fig. 4(a), the wave packets at top and bottom edges exhibit blue and red frequency shifts, verifying that it is of Type-I. Note that the frequency shifting amounts are different, implying the different amplitudes of group velocity for the two surface states. On the contrary, the packets at two edges both exhibit blue frequency shifts in Fig. 4(b), showing that it is of Type-II. In Fig. 4(c), we consider
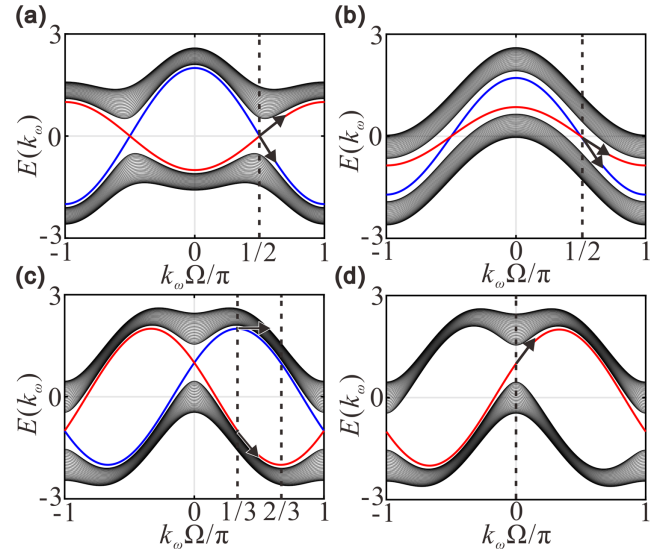
Fig. 3. Sliced band structures at $k_x = 0.85\pi/\sqrt{a}$ of the "zz" lattice for (a)–(c) and the "zb" lattice for (d). (a) and (b) denote the P-broken case and (c) and (d) are the T-broken cases. The black curves denote the bulk bands, and the red (blue) curves denote the surface states with the black arrows denoting the group velocities.
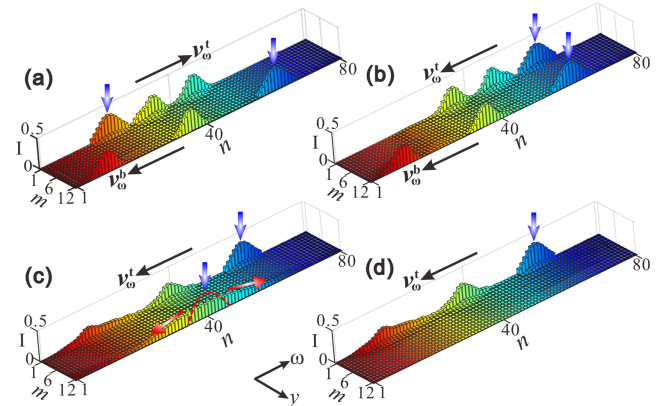

Fig. 4. (a), (b) Frequency evolutions of surface states wave packets for the Type-I and Type-II WSMs at $k_\omega = 0.508\pi/\Omega$ in the "zz" lattice. The blue arrows denote the initial positions, v_ω^t and v_ω^b are group velocities in frequency dimension with the black arrows denoting the directions. (c) Spectrum shifts and band expansion at $k_\omega = \pi/3\,\Omega$ of two surface states for the T-broken case. The red dashed curve and arrows represent the input packet and expansion directions. (d) Frequency evolution of the single surface states for the "zb" lattice.

the T-broken case, where the packet carries the critical-point Bloch momentum $k_\omega = \pi/3\Omega$. It shows that the spectrum of surface state at top edge keeps shifting while it is fixed at bottom edge, showing the signature of the vanishing group velocity. The packet expansion is due to the nonzero group velocity dispersion $\mathrm{GVD} = \partial^2 E(q)/\partial q_\omega^2 \neq 0$. Additionally, in Fig. 4(d), we simulate the surface state evolution for the "zb" lattice, the most prominent signature is that there only exists one surface state shifting along the frequency axis.

Up to now, we consider the frequency evolution of surface states in a single Weyl lattice, below we consider the frequency refraction in a composited waveguide array by cascading Type-I
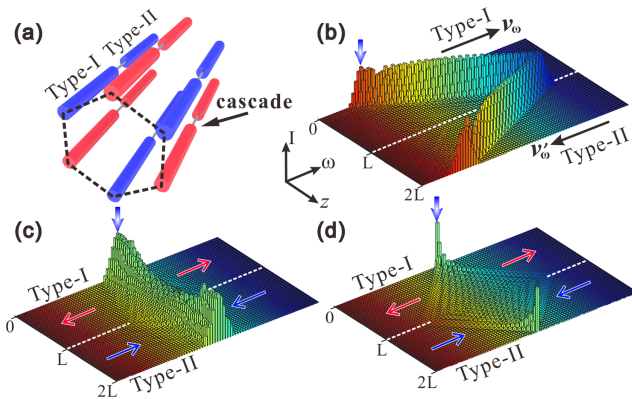
Fig. 5. (a) Schematic of cascaded dynamically modulated waveguide arrays of the Type-I and Type-II WSMs. (b) Frequency negative refraction for a wave packet input. v_ω and v'_ω denote the group velocities along frequency dimension in the two parts. (c) Spectrum expansion and compression for the packet input. (d) Spectrum perfect imaging for a single frequency input.

Weyl lattices and Type-II Weyl lattices. As shown in Fig. 5(a), the cascading system can enable time-reversed frequency evolutions of surface states, such as the "negative refraction" and "bandwidth expansion-compression" for wave packet and "perfect imaging" for a single frequency input. Figure 5(b) displays the refraction process of a spectrum wave packet with a center Bloch momentum $k_\omega = 0.508\pi/\Omega$ and launched at the top edge of the lattice with $z = 0$. The packet exhibits red frequency shift in the first Type-I lattice and manifests a negative refraction at the interface with $z = L$ and then exhibits blue frequency shift in the second Type-II lattice. Such a negative refraction process is due to the band slope flip of the surface state from Type-I to Type-II, as shown in Figs. 3(a) and 3(b), respectively.

Figure 5(c) displays the results of bandwidth expansion and compression. The center Bloch momentum of the injected wave packet now is set as $k_\omega = 0$. Since $k_\omega = 0$, the group velocity in the frequency dimension vanishes but the GVD is nonzero. The GVD also exhibits a flip when Weyl phase transition occurs, i.e., GVD > 0 in the first array and GVD < 0 in the second. Therefore, the frequency spectrum is broadened in the first array and compressed in the second. The process of perfect imaging is depicted in Fig. 5(d), where the input signal is a single frequency. The single frequency could be regarded as the composition of frequency comb with Bloch momentum k_ω covering the entire Brillouin zone. Therefore, each frequency comb undergoes negative refraction in the process of propagation, leading to the perfect focusing on a single frequency.

In summary, we demonstrate the frequency manipulations of topological surface states through Weyl phase transitions in the dynamically modulated honeycomb waveguide arrays. We show that the topological surface state pairs exhibit unidirectional and bidirectional frequency shifts for Type-I WSMs and Type-II WSMs. Particularly, by cascading Type-I Weyl lattices and Type-II Weyl lattices together, we also achieve frequency negative refraction, bandwidth expansion-compression and perfect imaging. In experiment, the dynamic modulation could be realized by using four-wave mixing Bragg scattering (FWM-BS)

processes [23]. By injecting two pumped waves copropagating with a signal wave, the FWS-BS can give rise to successive frequency conversions of signal light, forming a frequency lattice with lattice constant determined by the two pumped waves frequency interval $\Omega = \omega_{p2} - \omega_{p1}$. Then the two WSM phases can be realized by controlling the amplitudes and phases of two pumped waves. Our works offer new approaches to manipulate the frequency of topological states, which may find applications in signal processing and optical communication.

Disclosures. The authors declare no conflicts of interest.

Data Availability. Date underlying the results presented in this Letter are not publicly available at this time but may be obtained from the authors upon reasonable request.

REFERENCES

1. X. Wan, A. M. Turner, A. Vishwanath, and S. Y. Savrasov, Phys. Rev. B **83**, 205101 (2011).
2. B. Q. Lv, H. M. Weng, B. B. Fu, X. P. Wang, H. Miao, J. Ma, P. Richard, X. C. Huang, L. X. Zhao, G. F. Chen, Z. Fang, X. Dai, T. Qian, and H. Ding, Phys. Rev. X **5**, 031013 (2015).
3. L. Lu, L. Fu, J. D. Joannopoulos, and M. Soljačić, Nat. Photonics **7**, 294 (2013).
4. B. Yang, Q. Guo, B. Tremain, L. E. Barr, W. Gao, H. Liu, B. Beri, Y. Xiang, D. Fan, A. P. Hibbins, and S. Zhang, Nat. Commun. **8**, 97 (2017).
5. Q. Wang, Y. Ge, H. X. Sun, H. Xue, D. Jia, Y. J. Guan, S. Q. Yuan, B. Zhang, and Y. D. Chong, Nat. Commun. **12**, 3654 (2021).
6. M. Xiao, W.-J. Chen, W.-Y. He, and C. T. Chan, Nat. Phys. **11**, 920 (2015).
7. A. A. Soluyanov, D. Gresch, Z. Wang, Q. Wu, M. Troyer, X. Dai, and B. A. Bernevig, Nature **527**, 495 (2015).
8. M. Trescher, B. Sbierski, P. W. Brouwer, and E. J. Bergholtz, Phys. Rev. B **91**, 115135 (2015).
9. Z. Wang and S.-C. Zhang, Phys. Rev. B **87**, 161107 (2013).
10. J. Lavoie, J. M. Donohue, L. G. Wright, A. Fedrizzi, and K. J. Resch, Nat. Photonics **7**, 363 (2013).
11. T. Kobayashi, R. Ikuta, S. Yasui, S. Miki, T. Yamashita, H. Terai, T. Yamamoto, M. Koashi, and N. Imoto, Nat. Photonics **10**, 441 (2016).
12. T. Udem, R. Holzwarth, and T. W. Hänsch, Nature **416**, 233 (2002).
13. S. Zaske, A. Lenhard, C. A. Kessler, J. Kettler, C. Hepp, C. Arend, R. Albrecht, W. M. Schulz, M. Jetter, P. Michler, and C. Becher, Phys. Rev. Lett. **109**, 147404 (2012).
14. C. Qin, F. Zhou, Y. Peng, D. Sounas, X. Zhu, B. Wang, J. Dong, X. Zhang, A. Alu, and P. Lu, Phys. Rev. Lett. **120**, 133901 (2018).
15. L. Yuan and S. Fan, Optica **3**, 1014 (2016).
16. H. Chen, N. Yang, C. Qin, W. Li, B. Wang, T. Han, C. Zhang, W. Liu, K. Wang, H. Long, X. Zhang, and P. Lu, Light Sci. Appl. **10**, 48 (2021).
17. A. Dutt, M. Minkov, Q. Lin, L. Yuan, D. A. B. Miller, and S. Fan, Nat. Commun. **10**, 3122 (2019).
18. L. Yuan, Y. Shi, and S. Fan, Opt. Lett. **41**, 741 (2016).
19. Q. Lin, M. Xiao, L. Yuan, and S. Fan, Nat. Commun. **7**, 13731 (2016).
20. C. Qin, Q. Liu, B. Wang, and P. Lu, Opt. Express **26**, 20929 (2018).
21. T. Ozawa, H. M. Price, A. Amo, N. Goldman, M. Hafezi, L. Lu, M. C. Rechtsman, D. Schuster, J. Simon, O. Zilberberg, and I. Carusotto, Rev. Mod. Phys. **91**, 015006 (2019).
22. Y. Plotnik, M. C. Rechtsman, D. Song, M. Heinrich, J. M. Zeuner, S. Nolte, Y. Lumer, N. Malkova, J. Xu, A. Szameit, Z. Chen, and M. Segev, Nat. Mater. **13**, 57 (2014).
23. W. Li, C. Qin, T. Han, H. Chen, B. Wang, and P. Lu, Opt. Lett. **44**, 5430 (2019).